DNS of unsteady shock boundary layer interaction

Suman Muppidi [*]& Krishnan Mahesh [†]

Aerospace Engineering & Mechanics

University of Minnesota

A novel numerical scheme has been developed to simulate high speed viscous flows in complex geometries using unstructured grids. A characteristic–filter based shock capturing scheme is applied as a corrector step to a non–dissipative predictor scheme. This algorithm is being used to study shock turbulent boundary layer interactions and this paper presents the results of a turbulent flow at Mach 2.9 over a 24° compression corner. Turbulent boundary layer flow is generated by a natural laminar–turbulent transition using a roughness strip. This methodology results in a fully developed turbulent boundary layer which shows good agreement with available data. The solution of the compression corner flow is compared to experiments at similar conditions and the agreement is reasonable. An examination of the wall pressure signal shows the low frequency behavior characteristic of this problem. Simulations show that the shock affects the transition location and the skin friction coefficient of the incoming boundary layer.

I.   Introduction

Shock wave boundary layer interactions can significantly alter the aerodynamic and thermodynamic loads in high speed flight. Figure 1 shows schematics of two canonical shock boundary layer interaction problems – impinging shock and compression corner. The flow fields are characterized by strong pressure gradient, separation, and unsteadiness. The interaction between the compressible effects (dependent mainly on the Mach number) and the viscous effects (a function of the Reynolds number) makes the problem challenging. Comprehensive reviews of the flowfield, and the predictive capabilities are presented in Delery & Panaras (1996), Knight & Degrez (1998), Dolling (2001), Knight et al (2003), and Edwards (2008).

Reynolds–averaged Navier–Stokes (RANS) simulations of this problem do not capture the unsteadiness exhibited by this flow, even as they capture the mean pressure distribution reasonably well (Knight and Degrez 1998, Knight et al 2003). As a result, RANS predictions of fluctuating aerodynamic and thermodynamic loads are generally inadequate. Direct Numerical, and Large Eddy Simulations of shock wave boundary layer interactions are fairly recent (eg: Urbin et al 1999, Adams 2000, Rizzetta & Visbal 2001, Kannepalli et al 2002, Pirozzoli & Grasso 2006, Loginov et al 2006, Wu & Martin 2007). In addition to large computational meshes to resolve the small–scale features, high–fidelity numerical techniques are necessary to accurately simulate/predict this problem. While shock capturing schemes are inherently dissipative, a good turbulent flow solution requires that the algorithm be non–dissipative.

Most past work on shock boundary layer interaction has used structured grid solvers, which can not be easily extended to complex geometries. The present study is aimed at developing solvers capable of handling unstructured meshes which can be used on engineering geometries. An algorithm to simulate compressible flows on unstructured grids was developed by Park & Mahesh (2007). It solves the compressible Navier–Stokes equations using a finite volume approach, and employs a modified least–squares approach to reconstruct the fluxes at cell faces (that makes the convective flux computation more accurate), and a scheme to split the viscous stress tensor into the compressible and the incompressible parts (that makes the viscous flux computation efficient). A characteristic filter based shock capturing scheme provides stable solutions in the presence of discontinuities. The filter is designed to be active only in the vicinity of the shock, hence not adding any numerical dissipation in regions away from shocks (in the turbulent regions of the boundary layer, for example).

---

[*]Research associate, Aerospace Engineering & Mechanics, AIAA member

[†]Professor, Aerospace Engineering & Mechanics, AIAA Associate Fellow

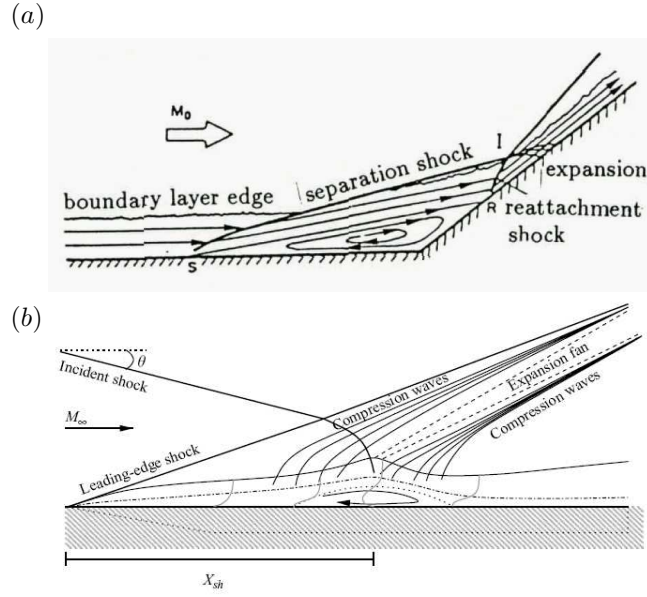American Institute of Aeronautics and Astronautics

(a)

(b)

Figure 1. Schematic of the flowfield resulting from (a)supersonic ramp flow (reproduced from Delery & Panaras 1996), and (b)shock wave incident on a boundary layer (reproduced from Robinet 2007).

The purpose of the paper is to evaluate the algorithm and methodology for studying high speed turbulent flows by simulating a Mach 2.9 turbulent flow past a 24° compression corner. Upstream boundary layer flow is generated by inducing transition in a laminar flow instead of a rescaling–type mechanism used in earlier simulations (Urbin et al 1999, Adams 2000, Wu & Martin 2007). The paper is organized as follows. The algorithm is presented in section II, and the problem setup is described in section III. The incoming turbulent flow is validated in section IV A and the flow past the compression corner is presented in section IV B. This section includes comparison to existing results. Section IV C presents data to show how the compression corner affects the boundary layer upstream. The unsteadiness in the separation region is described in section IV D, and the paper ends with a short summary in section V.

II.   Numerical Details

The algorithm solves the compressible Navier–Stokes equations on unstructured grids. The governing equations are

$$
\begin{aligned}
\frac{\partial \rho}{\partial t} &= -\frac{\partial}{\partial x_k}\left(\rho u_k\right), \\
\frac{\partial \rho u_i}{\partial t} &= -\frac{\partial}{\partial x_k}\left(\rho u_i u_k + p\delta_{ik} - \sigma_{ik}\right), \text{ and} \\
\frac{\partial E_T}{\partial t} &= -\frac{\partial}{\partial x_k}\left\{\left(E_T + p\right)u_k - \sigma_{ik}u_i - Q_k\right\},
\end{aligned}
\tag{1}
$$

where ρ, u_i, p and E_T are density, velocity, pressure and total energy, respectively. The viscous stress σ_{ij} and heat flux Q_i are given by

$$
\sigma_{ij} = \frac{\mu}{Re}\left(\frac{\partial u_i}{\partial x_j} + \frac{\partial u_j}{\partial x_i} - \frac{2}{3}\frac{\partial u_k}{\partial x_k}\delta_{ij}\right),
\tag{2}
$$

$$
Q_i = \frac{\mu}{(\gamma - 1)M_\infty^2 RePr}\frac{\partial T}{\partial x_i}
\tag{3}
$$

after non-dimensionalization, where Re, M_∞ and Pr denote the Reynolds number, Mach number and Prandtl number respectively.

The governing equations are discretized using a cell–centered finite volume scheme. Upon integration over the control volume, application of the Gauss theorem, and some rearrangement, the governing equations may be written as
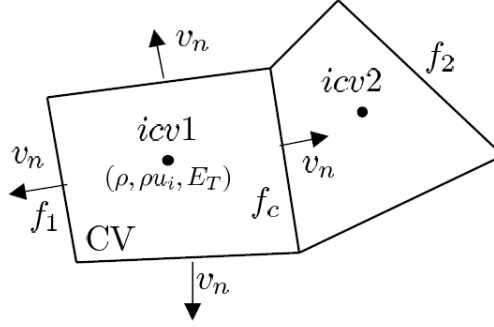
American Institute of Aeronautics and Astronautics

Figure 2. Schematic of the parallel faces on unstructured meshes, required for the shock capturing scheme. Computation of the filtered flux at face f_c requires information at faces f_1 and f_2.

$$
\begin{aligned}
\frac{\partial \rho_{\mathrm{cv}}}{\partial t} &= -\frac{1}{V_{\mathrm{cv}}} \sum_{\mathrm{faces}} \rho_f v_N A_f, \\
\frac{\partial (\rho u_i)_{\mathrm{cv}}}{\partial t} &= -\frac{1}{V_{\mathrm{cv}}} \sum_{\mathrm{faces}} \left[(\rho u_i)_f v_N + p_f n_i - \sigma_{ik,f} n_k \right] A_f, \\
\frac{\partial (E_T)_{\mathrm{cv}}}{\partial t} &= -\frac{1}{V_{\mathrm{cv}}} \sum_{\mathrm{faces}} \left[(E_T + p)_f v_N - \sigma_{ik,f} u_{i,f} n_k - Q_{k,f} n_k \right] A_f,
\end{aligned}
\tag{4}
$$

where V_{cv} is the volume of CV, A_f is the area of the face, n_i is the outward normal vector at surface, and v_N is the face-normal velocity. $\mathbf{q}_{\mathrm{cv}} = \left(\int_{\mathrm{cv}} \mathbf{q} dV \right) / V_{\mathrm{cv}}$ is the volume average within the cell, where $\mathbf{q} = (\rho, \rho u_i, E_T)$ is the vector of conservative variables. Here, the subscript f denotes interpolated values at each face of the control volume. Discretization of the governing equations involves reconstruction of the variables at the faces from the cell center values. Also, the spatial accuracy of the algorithm is sensitive to this flux reconstruction. The simulations employ a modified least–square method for this reconstruction, which can be shown to be more accurate than a simple symmetric reconstruction, and more stable than a least–square reconstruction. The algorithm uses a novel shock–capturing scheme that localizes numerical dissipation to the vicinity of flow discontinuities – thereby minimizing unnecessary dissipation. The solution is advanced in time using a second–order explicit Adams–Bashforth scheme, as

$$
q_j^{n+1} = q_j^n + \frac{\Delta t}{2} \left[3 \mathrm{rhs}_j(\mathbf{q}^n) - \mathrm{rhs}_j(\mathbf{q}^{n-1}) \right],
\tag{5}
$$

where rhs_j denotes j th component of r.h.s. of Eq. (4), and superscript n denotes n th time step. The algorithm has been used to solve a variety of problems, as presented in Park & Mahesh (2007).

The algorithm uses a shock–capturing scheme that was originally proposed by Yee et al (1999) for structured meshes and was extended by Park & Mahesh to unstructured meshes. Shock-capturing for non-dissipative schemes can be performed either by adding a filter, or hybridization with an upwind scheme. Here, the filtering technique is employed since the filter can be independently implemented with base scheme by predictor-corrector-like scheme. Once a physical time step Δt is advanced to get the solution $\hat{\mathbf{q}}^{n+1}$ from $\mathbf{q}^n$, the final solution $\mathbf{q}^{n+1}$ at $t + \Delta t$ is determined from a corrector-like scheme:

$$
\mathbf{q}_{\mathrm{cv}}^{n+1} = \hat{\mathbf{q}}_{\mathrm{cv}}^{n+1} - \frac{\Delta t}{V_{\mathrm{cv}}} \sum_{\mathrm{faces}} \left(\mathbf{F}_f^* \cdot \mathbf{n}_f \right) A_f,
\tag{6}
$$

where $\mathbf{F}_f^*$ is the filter numerical flux. $\mathbf{q}^n$ and $\mathbf{q}^{n+1}$ are the conserved variable arrays at time step n and $n+1$, and $\hat{\mathbf{q}}^{n+1}$ is the set of variables at time step $n+1$ but prior to the application of shock–capturing. The shock-capturing scheme is easily isolated from the base scheme and independent modification/refinement of each is possible. Unstructured grids do not always yield the information about variables at adjacent grid
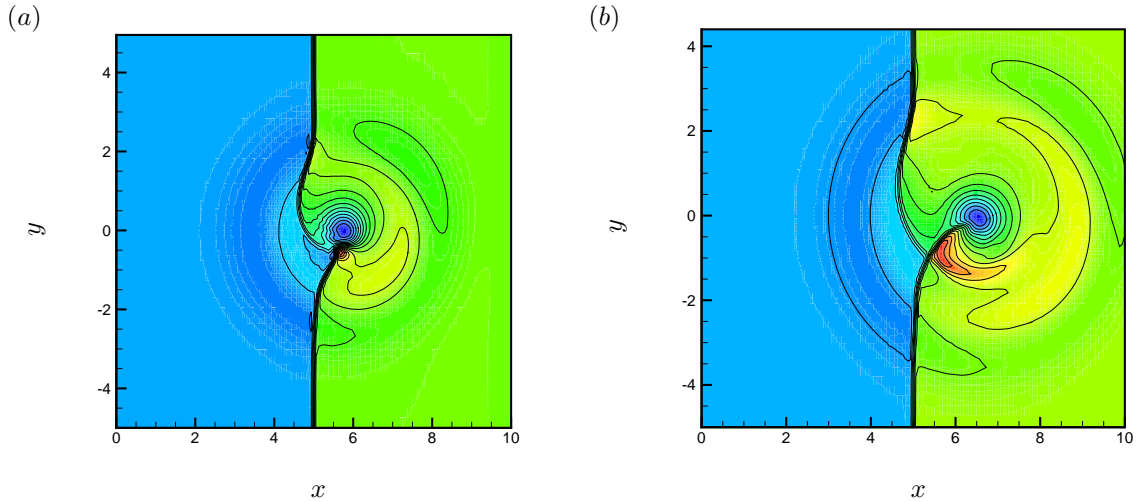
American Institute of Aeronautics and Astronautics

Figure 3. Figures show snapshots from the simulation of vortex convection through a normal shock using contours of pressure. Solution is shown at two different instances, vortex moves from left to right.

elements required in the original scheme (Yee et al 1999). This issue is resolved by using information at parallel faces f_1 and f_2 to compute the filtered fluxes at the face f_c (shown in figure 2), where f_1 (f_2) is defined as the most parallel face to f_c among all the faces f that surround $icv1$ ($icv2$) except for f_c itself. For a structured mesh, this formulation recovers the original scheme of Yee et al.

Shock Vortex Interaction Figure 3 shows contours of pressure from a simulation that showcases the features of the shock capturing scheme. A normal shock is set up at x=5.0, a vortex is at x=3.0 initially, and convects toward the shock. The figure shows the vortex at two different time instants as it passes through the shock. The interaction causes both the shock and the vortex to deform, as seem. The algorithm captures this deformation and resolves the shock. Importantly, any numerical dissipation is localized to the immediate vicinity of the discontinuity and the solution away from the shock sees no numerical dissipation. As the vortex convects downstream, the normal shock retains its original shape.

Laminar shock boundary layer interaction The algorithm was used to simulate a two–dimensional flow of a shock incident upon a boundary layer (a schematic of which is shown in figure 1b). The flow is from left to right at Mach 2.15, the angle of shock incidence is 30.8°, and the Reynolds number Re_{X_s} is 10^5 (X_s is the distance of the shock incidence location from the leading edge). Note that these conditions match the experiments of Degrez et al (1987). Figure 4(a) shows a snapshot from this simulation. Both the incident and reflected shocks are visible. The interaction causes the boundary layer to separate, as is also seen. In the experiment, the flat plate begins at $x/X_s = 0.0$, and the simulation replicates this geometry. As a result, one observes an oblique shock originating from the leading edge of the flat plate. Figure 4(b) also plots the variation of the wall pressure as a function of the streamwise distance along with the experimental results. The agreement is reasonable. At these conditions, both the simulation and the experiment result in a steady flow. However, as the Reynolds number is increased by a factor of 10, the solution becomes unsteady. The unsteadiness originates in the interaction region and travels both upstream and downstream. Figure 4(c) shows a snapshot from the solution at this higher Reynolds number, and the unsteady interaction is apparent. Figures 4(a) and (c) indicate that the algorithm/solution exhibits the desired sensitivity to Reynolds number. The solution also indicates that the interaction between a shock and boundary layer has a certain tendency to become unsteady at the right conditions. Finally, at these Reynolds numbers, the unsteadiness propagates upstream and this example, the influence is felt all the way upto the leading edge of the boundary layer.

This unsteadiness imposes a challenge to simulating shock boundary layer interaction problems. Figure 5 shows contours of Cartesian velocity v from the simulation of a two–dimensional supersonic flow (Mach 2.9) past a 24° compression corner. Note that the interaction region is unsteady. The oblique shock due to the wedge imposes an adverse pressure gradient, and the unsteadiness travels upstream. In this example, the computational inflow is at x=4.0. If the inflow were closer to the corner (say, at x=6 or 7), results show the presence of a strong leading edge shock at the inflow due to the combination of the upstream propagating

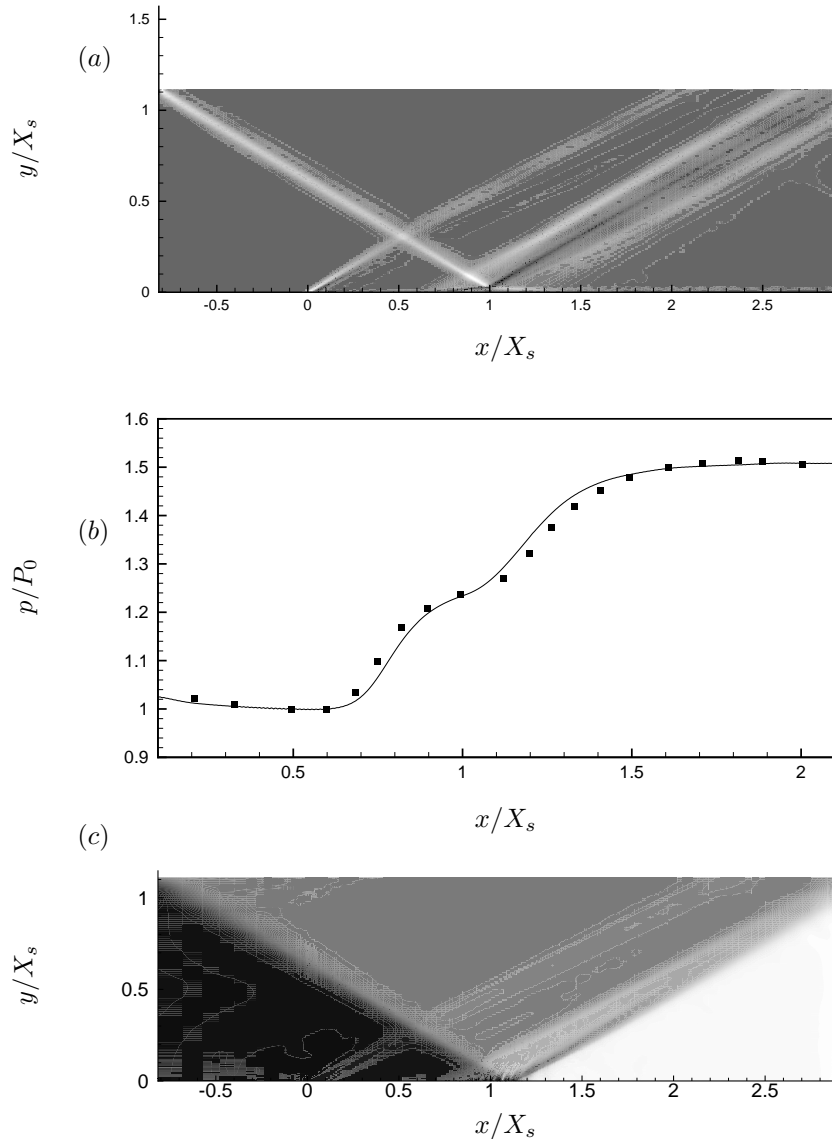American Institute of Aeronautics and Astronautics

Figure 4. Interaction of an incident shock with a laminar boundary layer. (a) shows an instantaneous numerical Schlieren at experimental conditions of Degrez et al (1987). The flow is steady. (b) shows wall pressure variation (lines - present simulation, symbols - experiment). Note that the comparison is reasonable. (c) Snapshot from the simulation with 10 times the Reynolds number as in the experiment. At this Re, the interaction is unsteady, and the unsteadiness propagates upstream, upto the leading edge of the boundary layer.
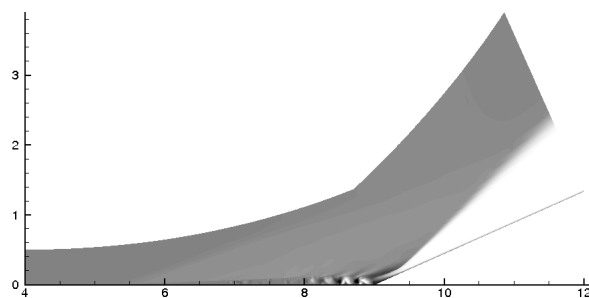

Figure 5. Snapshot of a two–dimensional supersonic flow past a ramp. The flow is unsteady, and influence of the unsteady separation region is felt on the laminar boundary layer upto a significant distance upstream.
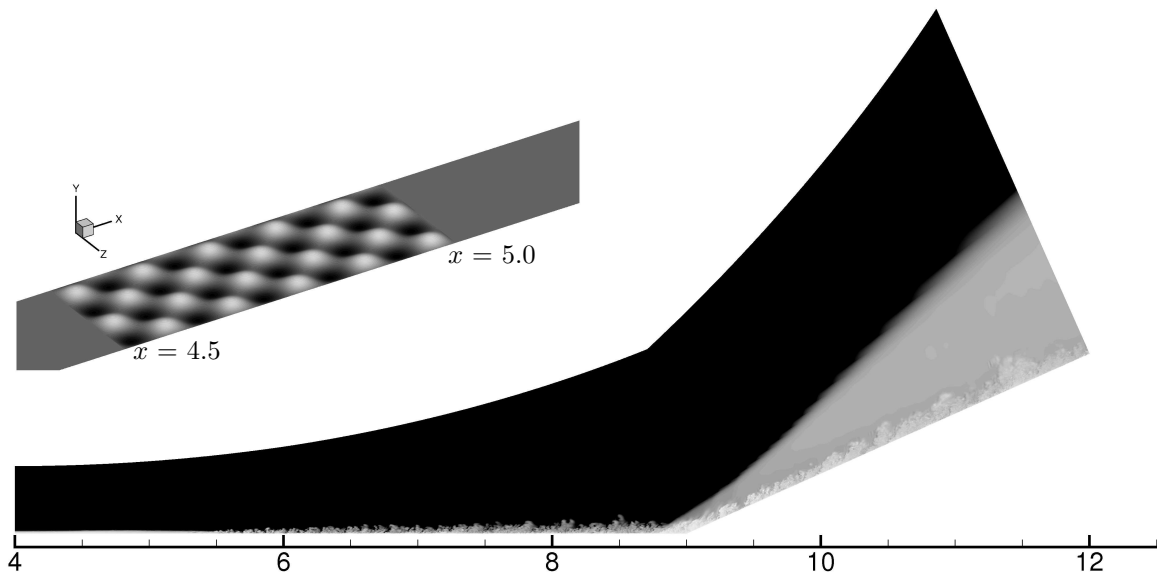
American Institute of Aeronautics and Astronautics

Figure 6. Schematic of the the simulation setup. Figure in the inset shows a closer view of the roughness strip.

unsteadiness and steady inflow boundary conditions. Clearly, this leading edge shock affects the solution, and the domain needs to be large enough to minimize this upstream influence. This is not an issue in a geometry such as shown in figure 4 since the leading edge of the boundary layer is downstream of the domain inflow, and upstream propagating unsteadiness extends only up to the leading edge.

III.   Simulation setup

The objective of the present paper is to simulate and study turbulent supersonic flow past a compression corner. A well-known challenge in this simulation is the specification of realistic inflow data. Various methodologies have been used, and are described in the literature. Adams (2000) and Loginov et al (2006) perform a separate DNS of a spatially evolving zero pressure gradient turbulent flat plate boundary layer, which was then interpolated onto the inflow plane of the compression corner simulation. This flat plate DNS itself required an inflow which was obtained from yet another temporal DNS calculation. In order to match the boundary layer parameters at a reference location with that of the experiments, Loginov et al use a rescaling technique. Rescaling–type inflow generation methods are highly popular, and have been used by Urbin et al (1999) and Wu & Martin (2007) among others. Priebe & Martin (2010) observe that over long solution time, a DNS using rescaling methods is susceptible to an acoustic mode in the freestream – as seen by the growth in freestream fluctuations over time. Priebe & Martin apply a flow filter in the freestream to damp these fluctuations. Morgan et al (2010) observe that the standard recycling/rescaling scheme introduces non–physical 'tones' into the inflow and contaminates the solution, and use an improved rescaling method to simulate a turbulent boundary layer interacting with an impinging shock.

The present study uses roughness–induced transition to generate turbulent inflow upstream of the compression corner. This methodology avoids any rescaling as well as any unphysical forcing of the turbulent flow. A schematic of the problem is shown in figure 6. The incoming flow ($x = 4.0$ inches) is a laminar boundary layer at Mach 2.9 specified according to the similarity solution for compressible flows (Schlichting 1963) such that the origin of the boundary layer is at $x = 0$ (the incoming boundary layer thickness is $\delta_{inflow} \sim 0.02$ inches, and the unit Reynolds number is 635000/inch). A roughness strip along the wall ($4.5 \leq x \leq 5.0$) induces transition resulting in the flow becoming turbulent. A 24 degree wedge is located at $x = 9.0$, and the present simulations (both with and without the ramp) indicate that the flow becomes fully turbulent by $x = 6.0$, well upstream of the corner. The figure in the inset shows the roughness region whose height varies sinusoidally in x and z.

Periodic boundary conditions are applied at the spanwise boundaries (spanwise extent of the domain is

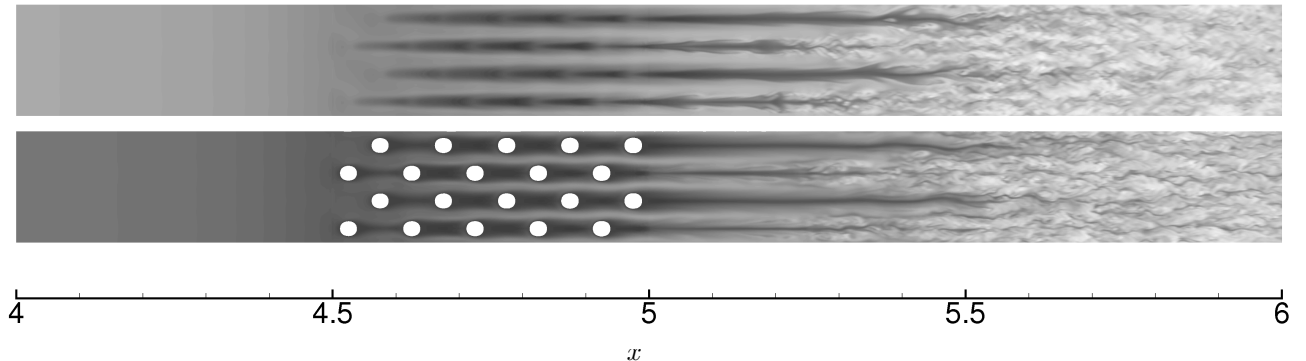American Institute of Aeronautics and Astronautics

Figure 7. A snapshot of the flow close to the transition region using contours of streamwise velocity. Figure shows two planes on either side of the peak roughness height.

0.175 inches), and a zero–gradient boundary condition is applied at the top and outflow boundaries. Note that the shock exits the domain cleanly. At the wall, no slip boundary conditions for velocity, isothermal condition for temperature ($T_{wall} = T_{adiabatic}$) and zero–gradient boundary condition for pressure are applied. Sutherland's formula is used to compute viscosity as a function of the temperature. The computational mesh consists of nearly 60 million hexahedral elements, distributed evenly in the wall–parallel and spanwise directions, and clustered near the wall in the wall–normal direction.

IV.   Results

A.   Turbulent flow upstream of the corner

The present simulations achieve turbulent flow by causing incoming laminar flow to become turbulent. Transition is induced by a region of roughness on the flat plate, described as a sinusoidally varying surface $y_{wall} = h\, sin(k_1 x) sin(k_2 z)$ where h is 0.0075 inches. The local h/δ is around 0.35. Figure 7 shows snapshots of the flowfield using contours of streamwise velocity on wall–parallel planes at two locations $y = 0.005$ and 0.01 inches. Note that the incoming two–dimensional laminar flow is perturbed by the roughness strip. Streamwise streaks of alternating high and low velocities are observed. These streaks break down and the flow appears highly unsteady, three–dimensional, and turbulent by $x = 5.5$. It may be observed that the low speed streaks are due to the deceleration of streamwise flow caused by the roughness/obstacle, and the high speed streaks are due to the acceleration of fluid between the roughness elements.

A quantitative indication of the transition is provided by figure 8 which shows the variation of skin friction coefficient C_f and the turbulent kinetic energy along the wall. C_f values begins to rise shortly downstream of the roughness strip indicating transition, reach a peak close to $x = 6.0$ and decrease gradually thereafter. Turbulent kinetic energy shows a similar behavior. The flow is completely steady up until about $x = 5.5$ (past the roughness strip), and shows an increase between 5.5 and 6.0 where a peak is observed. These curves are obtained by averaging across the span.

Figure 9 presents profiles of VanDriest transformed velocity as a function of the wall normal distance at a few stations along the streamwise distance. Van Driest velocity is computed as:

$$u_{VD}(y) = \int_0^u \sqrt{\frac{\rho}{\rho_{wall}}}\, du \; ,$$

and plotted as a function of the wall normal distance in wall units. The profiles are compared to existing numerical and experimental data. Note that the experimental data of Ringuette et (2009) comprises of two curves; the hollow symbols correspond to the original data and the filled symbols are obtained by 'shifting' the velocity profiles that fall below y^+ of 62. Details are given in Ringuette et al. The experimental data of Zheltovodov et al (1990) is taken from Loginov et al (2006). The hollow symbols in this case again correspond to the original data, and the filled symbols were obtained by scaling the dimensional experimental data with
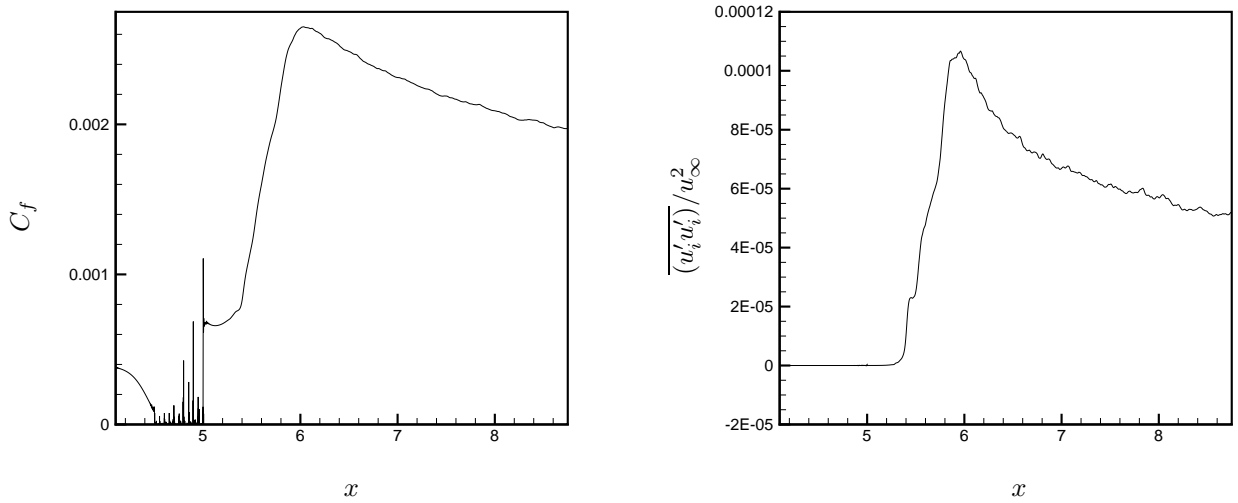
American Institute of Aeronautics and Astronautics

Figure 8. Variation of skin friction coefficient and turbulent kinetic energy along the wall. Note that the flow begins to transition past the roughness strip.

the friction velocity of LES by Loginov et al. The DNS data of Wu & Martin (2007)has been extracted from Ringuette et al. The relevant characteristic parameters describing these data sets are presented in table 1, along with the reported values for skin friction coefficient (figure 8) and the shape factor (figure 12) where reported.

Reference	Mach number	Re_θ	C_f	Shape factor H
Guarini et al (2000)	2.5	1577	0.00282	
Gatski & Erlebacher (2002)	2.25	4250		
Loginov et al (2006)	2.95	2046	0.00205	5.19
Wu & Martin (2007)	2.9	2400	0.00217	4.74
Bookey et al (2005)	2.9	2400	0.00225	5.51
Ringuette et al (2009)	2.9	2400	0.00217	5.49
Zheltovodov et al (1990)	2.95	1826	0.00179	5.3

Table 1. Relevant parameters of simulations and experiments that the present turbulent boundary layer are compared against, in figure 9. See original references for the definition of Re_θ.

Figure 10 presents a few more comparisons using data from Bookey et al (2005), Ringuette et al (2009), and those reported in Loginov et al (2006). Profiles of streamwise velocity u, density ρ, temperature T and Mach number M are plotted against y/δ, δ being the local boundary layer thickness (based on 99% u/u_∞). The agreement is reasonable, indicating that roughness-induced transition results in a fully developed turbulent flow that compares well with available results. The comparisons also show that the flow is turbulent far upstream of the corner. By $x = 6.5$, for example, the profiles appear turbulent and show good agreement (figure 10). Lastly, transition appears to begin away from the wall (as seen by the unsteadiness in the snapshots, figure 7), and is reflected slightly downstream in the skin friction curves. This observation reflects the inherent difficulty in characterizing a 'transition location' for unsteady transitional flows.

The incoming boundary layer thickness is $\delta \sim 0.022$ inches, and is one length scale in this flow. This however, is specific to the problem setup. The length scale that allows comparison across different simulations/experiments is the boundary layer thickness at the location of the corner, in the absence of the corner, indicated here as δ_0. In the present case, δ_{inflow}/δ_0 is about 0.25. Figure 11 shows δ (computed as the y location of 99% u/u_∞) plotted against the streamwise distance starting from the end of the roughness strip to the location of the corner, from the simulation that did not include the corner. δ is normalized by δ_0. Past $x = 6.0$ where the flow becomes turbulent, δ rises steadily across the domain, and the difference is significant.
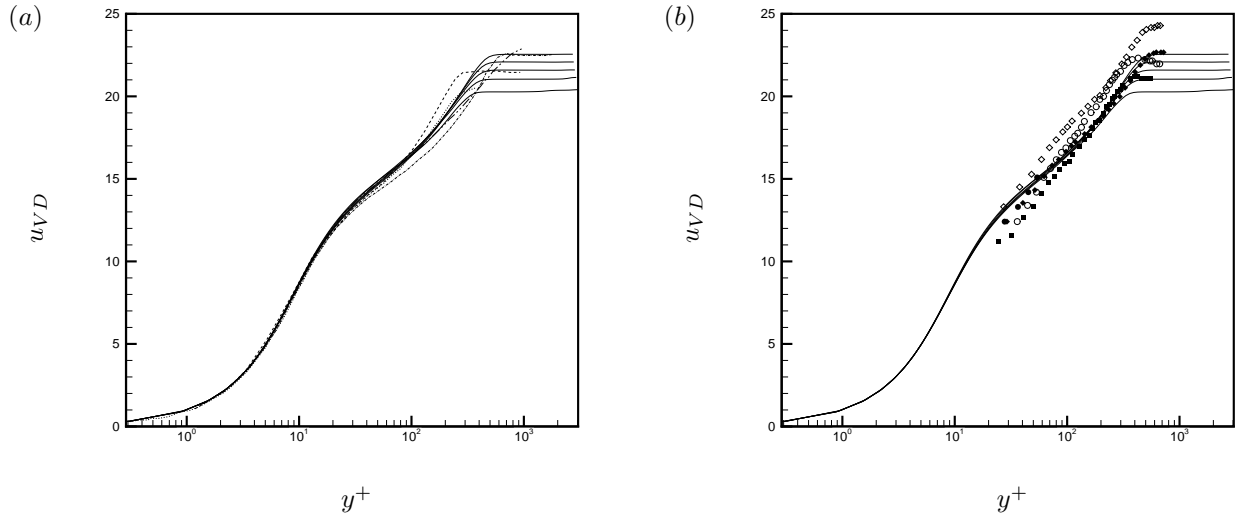
American Institute of Aeronautics and Astronautics

Figure 9. (a) Comparison of Van Driest transformed velocity profiles with available simulation data. Figure shows mean velocity profiles at locations $x = 6.5$, 7. 7.5, 8 and 8.5 (———) compared with profiles from simulations – Guarini et al[10] (········), Gatski & Erlebacher[9] (—··—), Wu & Martin[27] (- - - -) and Loginov et al[14] (—·—) (b) Comparison with experimental data. Bookey et al[3]($\blacksquare$), Ringuette et al[19] ($\bullet$), Zheltovodov et al[28] ($\blacklozenge$). The hollow symbols correspond to 'uncorrected' measurements (see text for details).

The figure also shows the variation of the Reynolds number based on the momentum thickness as a function of the streamwise distance. The two curves plot Re_θ computed using μ_{wall} and μ_∞. At the location of the corner, these Reynolds numbers are about 1800 and 3900 respectively. Note that the methodology for the present simulations does not allow a imposition of Re_θ, which a rescaling mechanism does. Instead, the boundary layer develops naturally and results in the Re_θ as shown in figure 11. Note that at the location of the corner, Re_θ (based on μ_∞) in the present simulations is higher than that of the experiments of Bookey et al and Ringuette et al, and the simulations of Wu & Martin.

B. Turbulent flow past compression corner

Figure 13 shows a snapshot of the flow on the symmetry plane across the whole domain using contours of density gradient magnitude. The turbulence in the boundary layer is clearly visible. Flow turns because of the corner, and results in an oblique shock that originates just upstream of the corner. The shock can be observed to penetrate the boundary layer, and the foot of the shock shows curvature as well as compression waves that travel in the streamwise direction. Figure 14 presents another visualization of the flow, using isosurfaces of Q criteria colored by contours of streamwise velocity. Note that only a part of the domain is shown, and the separation region is more apparent here than in figure 13. The shaded surface indicates the wall. Upstream of the corner, we observe flow features that are long and thin, and aligned in the streamwise direction. Closer to the corner, the velocity decreases as the flow turns. Past the corner, there is a change in the length scales, and the flow features are aligned at an angle to the wall. Figure 15 shows contours of Cartesian velocity u and temperature on planes parallel to the wall at three stations: $y =0.005$, 0.01 and 0.015. The figures extend only a small portion of the computational domain. The separated flow region is characterized by a decrease in u and an increase in temperature on all planes.

A well–known feature of this flow is the wall pressure variation in the interaction region. Settles al (1979) show the variation in wall pressure with distance for different wedge angles. At 8°, the transition from pre–shock pressure to a post–shock pressure is sharp, at the location of the corner. Where the ramp angle is 20°, the pressure curve shows a 'plateau' indicating separation region. As the ramp angle is increased to 24°, the pressure rise appears even farther upstream, and the pressure plateau extends over a larger streamwise extent. Past the corner, wall pressure increases toward the post–shock pressure. It may be observed that for 8 and 16° ramp angles, the observed post–shock pressure is very close to the inviscid value, while the difference is the greatest for the wedge angle of 24°. Figure 16 plots the wall pressure against streamwise

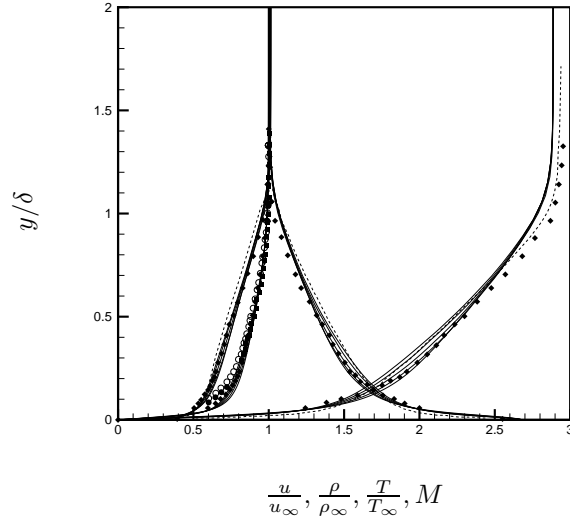American Institute of Aeronautics and Astronautics

Figure 10. Comparison of profiles of density, streamwise velocity, Temperature and Mach number across the boundary layer. Profiles from the present DNS correspond to $x = 6.5, 7. 7.5, 8$ and 8.5(———); Loginov et al[14] LES: —·— ; symbols from experiments - Bookey et al[3] (■), Zheltovodov et al[28] (♦), and Ringuette et al[28] (●).
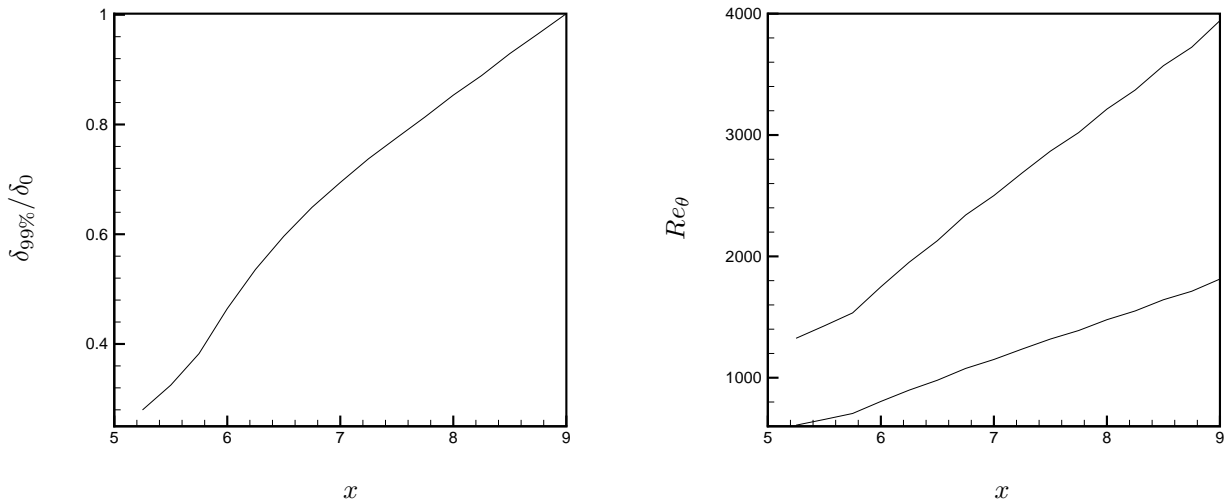

Figure 11. Variation of boundary layer thickness $\delta_{99\%}$ and Re_θ across the domain. δ_0 is the boundary layer thickness at the location of the corner, in the absence of the corner. The two curves correspond to Re_θ based on μ_{wall}, and on μ_∞.

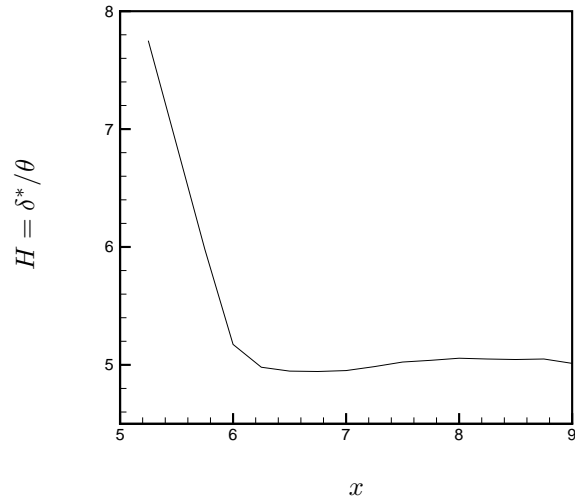American Institute of Aeronautics and Astronautics

Figure 12. Variation of the shape factor $H = \delta^*/\theta$ with the streamwise distance. Turbulent flow has a smaller H than the laminar one, and agrees reasonably with the values reported in table 1.
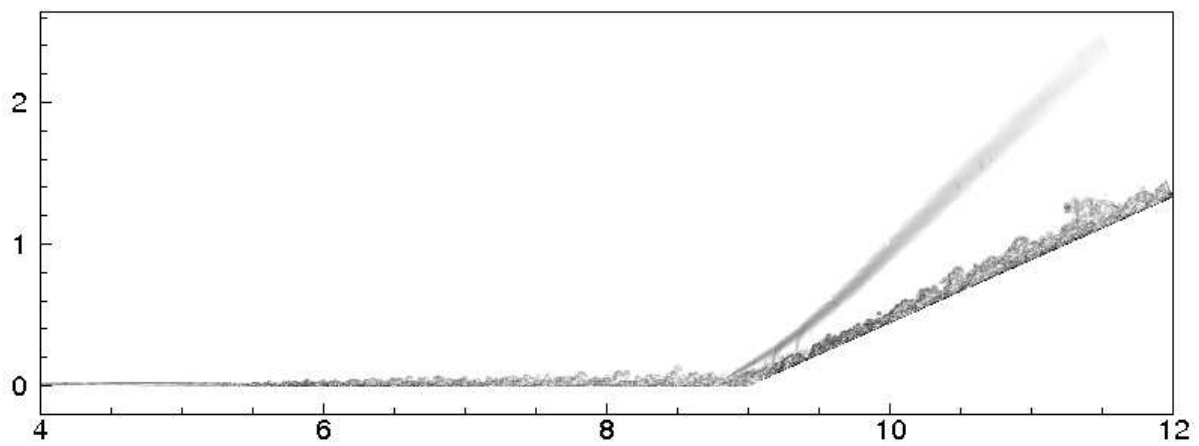

Figure 13. A snapshot of the flow using contours of density gradient magnitude.
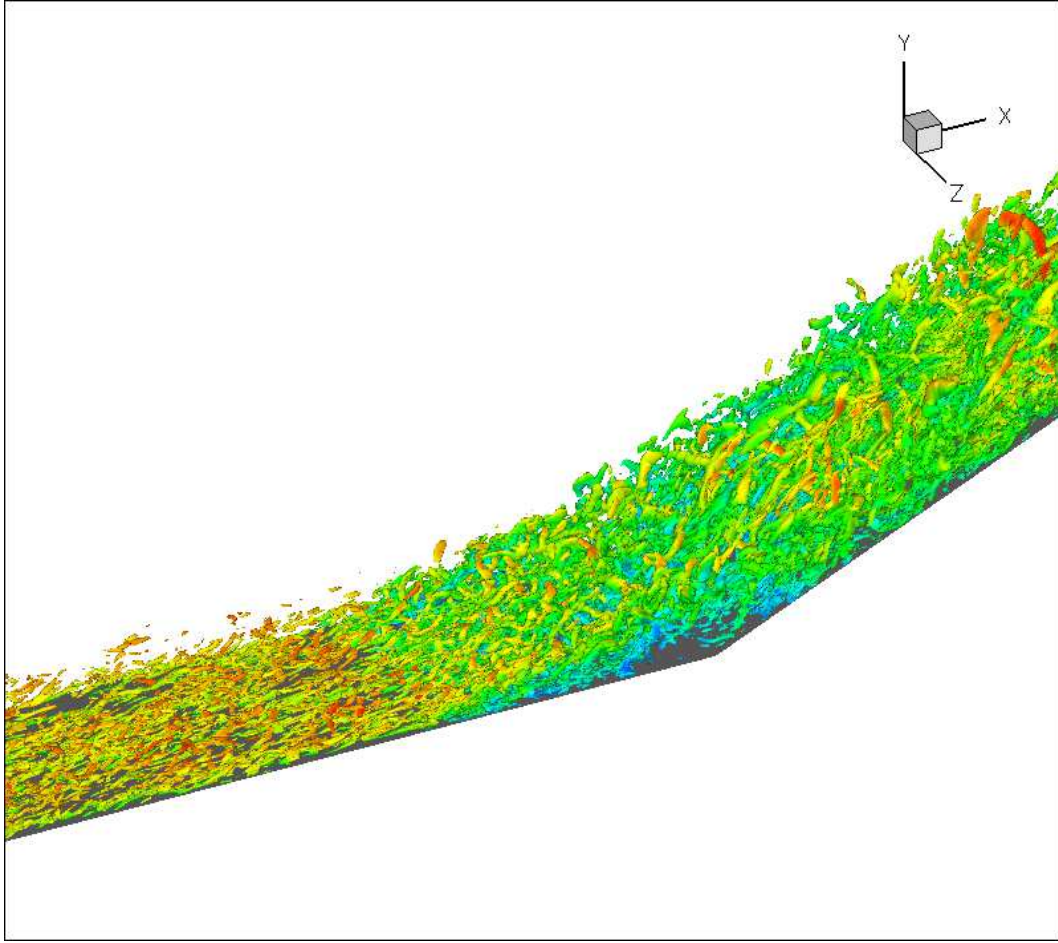
Figure 14. Iso surfaces of Q criteria, colored by streamwise velocity. Figure shows turbulence in the boundary layer and the change in length scales through the interaction region.

(Cartesian) distance from the present simulations. The solution shows an increase in wall pressure upstream of the corner, a plateau, and the recovery to the post–shock pressure downstream. The figure also shows experimental results from Bookey et al (2005), Ringuette et al (2009), Settles et al (1979), and DNS results of Wu & Martin (2007). Note that the agreement is reasonable. Figure 16 also shows the variation of pressure variance ($\sqrt{p'p'}/p_{wall}$) with streamwise distance. Available data from Ringuette et al and Wu & Martin (extracted from Ringuette et al) is also plotted for comparison. The curve shows a peak upstream of the corner, a decrease and another peak downstream of the corner. The increase in pressure variance is a consequence of the shock–foot motion (Loginov et al 2006). The peak $p'p'$ agrees reasonably with the experiment.

Figure 17 plots wall–parallel velocity with wall–normal distance at three streamwise stations $x = -5\delta_0$, $4\delta_0$, and $8\delta_0$. The velocity is normalized with the incoming freestream velocity u_∞, and the wall–normal distance with δ_0. The agreement is reasonable at the upstream station. The profiles from the simulation show higher momentum closer to the wall at the downstream stations. Ringuette et al state that near the wall, errors from the pitot tube can be significant. The velocity profile at $x = 4\delta_0$ has no reverse flow (attached), but shows region of low momentum close to the wall (momentum deficit). This is consistent with the experimental observation. At $x=8\delta_0$, the velocity profile shows a smaller deficit. Note the difference in values of Re_θ between the present simulation and the results of Ringuette et al, Bookey et al and Wu & Martin. This difference appears to result in a smaller separation region (figures 16) and greater near–wall momentum near the wall (figure 17), and is consistent with past observations.

Evolution of the mean flow along the domain is shown in figure 18 using wall–normal profiles of mean (wall–parallel) velocity and turbulent intensities at various x locations. The plots in the top row indicate

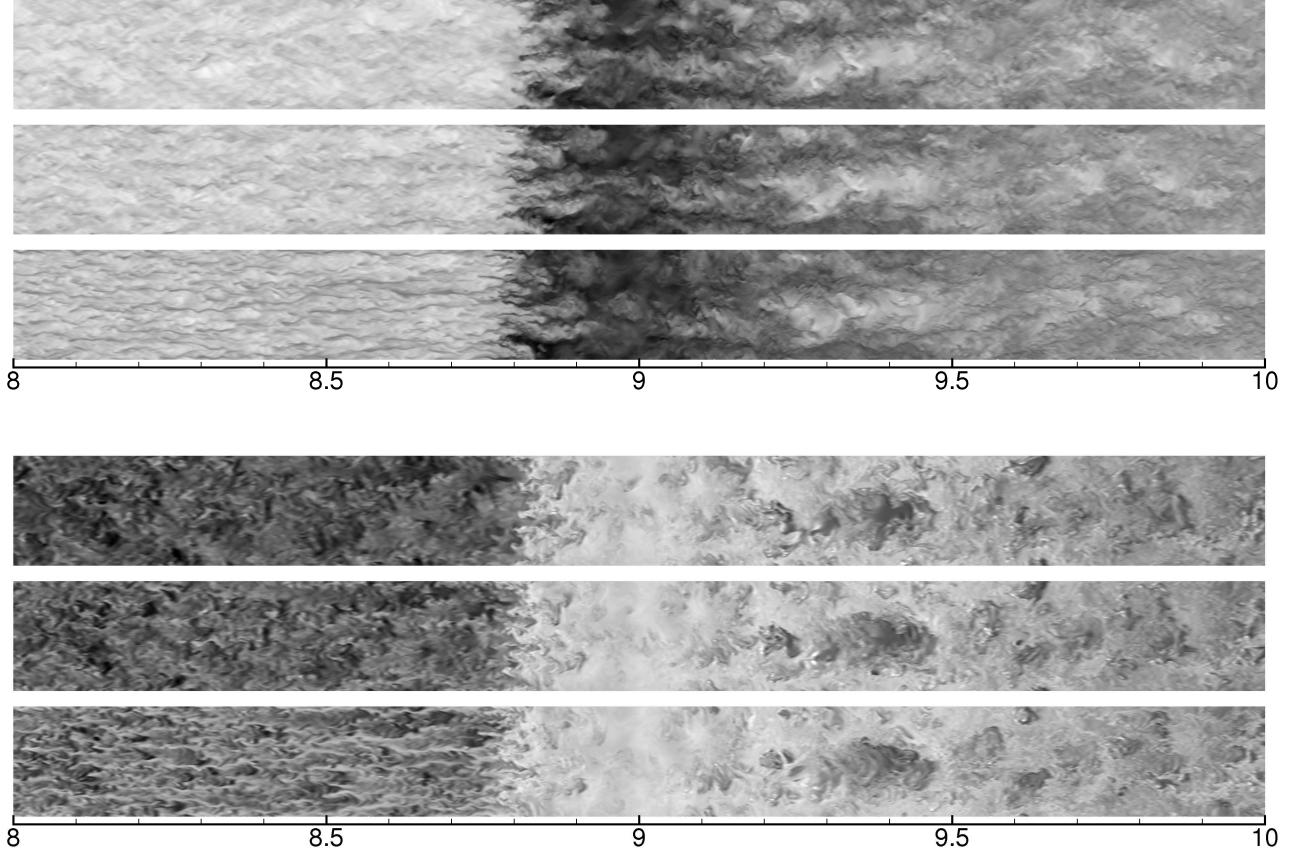American Institute of Aeronautics and Astronautics

Figure 15. Snapshots of the flow parallel to the wall using contours of Cartesian velocity u and temperature show the flowfield in the vicinity of the corner. The planes correspond to $y = 0.005$, 0.01 and 0.015 (bottom to top).

the location corresponding to each profile, as distance from the corner x_c. Up to and including $x_c = 0$, the wall–normal coordinate is the same as the Cartesian y coordinate. Thereafter, the profiles are taken normal to the wall and are hence at an angle of $24°$ with the Cartesian y axis. Mean velocity profiles at $x_c=-10\delta_0$ are similar to that expected of an undisturbed boundary layer. Closer to the corner, the flow begins to separate and the velocity profile indicates a decrease in the near–wall momentum. There is also a small reverse velocity observed. Past the corner, the velocity field recovers, and the profiles show an increase in the near–wall momentum and a filling up of the profile. Note that the peak velocity post–corner is less than the incoming streamwise velocity u_∞. The velocity profiles shown here are qualitatively similar to those presented in Loginov et al (2006), even as the exact locations of the profiles are different. One feature of this flow field is an increase in the turbulence through the shock, as presented by Smits & Muck (1987) and Andreopoulos et al (2000). Figure 18 shows this behavior using $\overline{u'u'}$ and $\overline{v'v'}$. The increase in turbulent intensities is significant starting at about $x_c = -3\delta_0$, and the location of the peak moves farther from the wall. The turbulent intensities remain high through the separation region and post–corner. Only by about $x = 10\delta_0$ do the intensity peaks appear to decrease back toward the pre–corner levels. Also, turbulent activity is observed over a significantly larger y_{normal} extent compared to the incoming flow.

C.   Effect of the ramp on the upstream turbulent flow

Section II showed the influence of the shock on the boundary layer using laminar two–dimensional simulations. In these examples, the upstream influence is felt in the form of unsteadiness propagating upstream, and an increased boundary layer thickness in the case of the compression corner flow. The present simulations include cases with and without the corner which isolate the influence of the shock/ramp on the turbulent
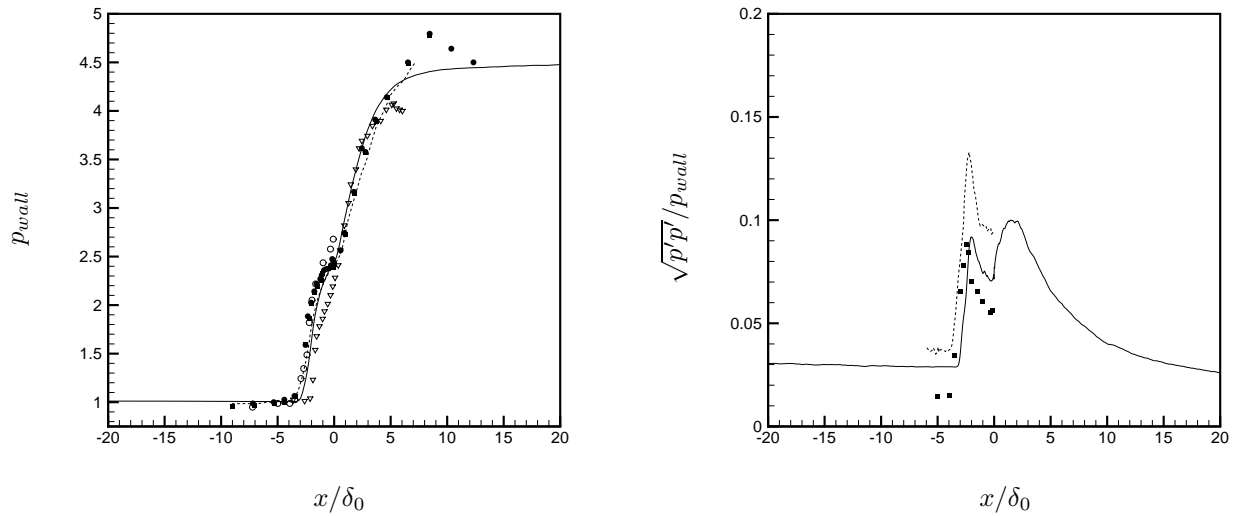
American Institute of Aeronautics and Astronautics

Figure 16. Comparison of mean and variance of wall pressure from the present simulations (———) compared with experiments of Bookey et al[3] (■), Ringuette et al[19] (● , ○), Settles et al[23] (▽) and DNS of Wu and Martin[27] (– – – –). This data is extracted from Bookey et al and Ringuette et al.

boundary layer. Figure 19 presents the variation of momentum based Reynolds number, and skin friction coefficient as a function of the streamwise distance from simulations with and without the compression corner. Both simulations are run at identical parameters, have the same exact roughness strip, and result in turbulent flow downstream of the roughness strip. The integral quantity θ and hence the Reynolds number Re_θ are observed to be different in the two cases. Near the corner, as flow separates, Re_θ variation ceases to be gradual, and can be ignored. The skin friction curve shows that in the presence of the corner, transition begins earlier, and the peak C_f value is reached earlier than in the case without the corner. Thereafter, both the curves decrease at different rates and over a large portion of the domain, the skin friction curves show a difference.

D. Separation region unsteadiness

The low frequency behavior in the separation region of shock boundary layer interaction has been the subject of many studies. The low frequency oscillations observed in the wall pressure measurements are considered to be a signal of the low frequency shock motion. Ringuette et al (2009) present wall pressure signals at different streamwise locations along with corresponding data from high Reynolds number experiments by Dolling & Murphy (1983), and DNS data of Wu & Martin (2007). It is observed that the high Reynolds number experiment shows significantly more intermittency – multiple jumps from the freestream levels to post–shock levels and back – attributed to the motion of shock above the pressure measurement location. Ringuette et al mention that at Re_θ of 2400, both the experiment and the DNS do not exhibit such intermittency, and the pressure signal is of a rather broader range of frequencies with a comparatively smaller amplitude than the high Reynolds number pressure signal. This is attributed to the fact that at the lower Reynolds number, the shock does not penetrate into the boundary layer.

Figure 20 presents time histories of wall pressure from the present DNS at a few different streamwise locations. The figure also shows a plot of the pressure and skin friction variation over the separation region. The vertical lines in the lower picture indicate the location of the pressure signal measurement. The most upstream location is $x=-3.4\delta_0$ where the mean pressure is the same as the incoming mean pressure, and the time history (blue) shows a fairly constant pressure with some smaller amplitude, high frequency behavior expected of a turbulent boundary layer. At $x=-2.27\delta_0$, the mean pressure begins to rise toward the plateau, indicating some degree of shock motion. Note that the skin friction at this location is negative indicating that this point lies downstream of the mean separation point. The pressure time history at this point (black) shows some evidence of low frequency behavior and is similar to the pressure signals of the DNS and experiment presented in Ringuette et al. The next pressure signal is at $x=-1.14\delta_0$, inside the separation
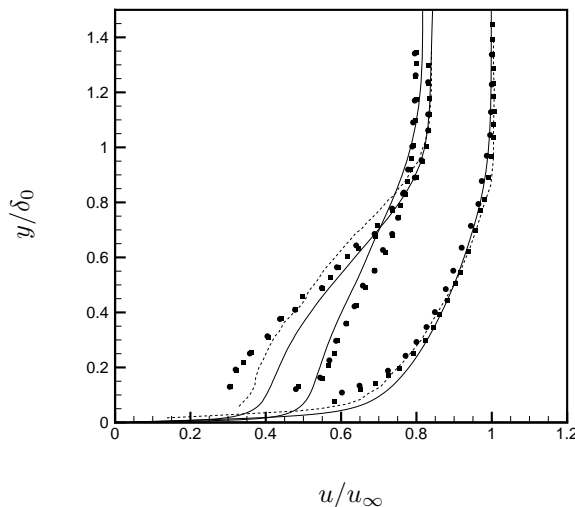
Figure 17. Variation of mean wall–parallel velocity with the wall–normal distance upstream and downstream of the corner. Results are compared against experimental values of Bookey et al[3] (■), Ringuette et al[19] (●) and simulations of Wu & Martin[27] (- - - -).

region and at about the middle of the pressure plateau. Shown in green, the mean pressure is higher but the low frequency behavior is still apparent. The signal at the most downstream location (shown in purple) belongs to the flow past reattachment point (positive C_f) and shows a mean pressure just slightly lower than the post–shock pressure.

V.   Conclusions

This paper presents a novel DNS/LES algorithm for solving high speed viscous flows in complex geometries, and our progress in using this algorithm towards simulating shock boundary layer interactions. We present results of a simulation of Mach 2.9 turbulent flow past a 24° compression corner. The simulation methodology involves the use of a roughness strip that causes the incoming laminar flow to transition and become turbulent upstream of the corner, thereby avoiding any rescaling–type turbulent inflow generation. Preliminary two–dimensional simulations indicate that at DNS accessible Reynolds numbers, the influence of the shock (pressure gradient) on the boundary layer can be felt far upstream. Even in a turbulent boundary layer, the measured skin friction and Reynolds numbers are different with and without the compression corner. The present simulations use a long computational domain to study this upstream influence. Detailed comparisons of the mean flow results from the simulation without a corner show good agreement with available simulation and experimental data at similar conditions. Contrary to other inflow generation methods, we are unable to 'specify' a Reynolds number; the flow transitions naturally and results in a turbulent boundary layer at some Reynolds number. It is observed that at the location of the corner, Re_θ is greater than in the experiments of Bookey et al 2005) and Ringuette et al (2009). Comparison of the compression corner profiles are found to be reasonable, with some differences which are consistent with the difference in Reynolds number.

VI.   Acknowledgments

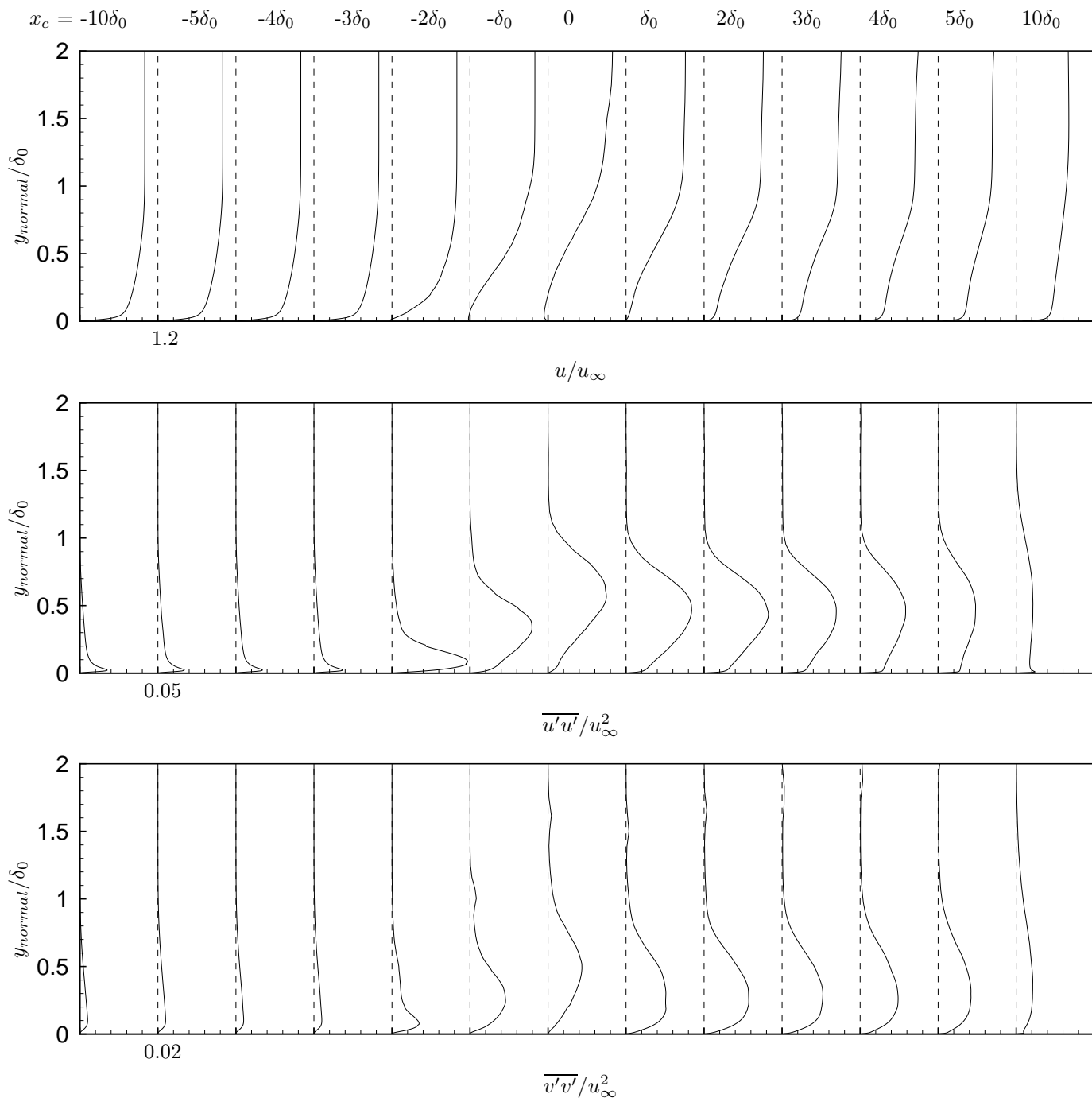American Institute of Aeronautics and Astronautics

Figure 18. Evolution of mean wall–parallel velocity (u) and turbulent intensities ($u'u'$ and $v'v'$) at various locations upstream and downstream of the corner. Numbers in the top row indicate the location of each profile along the wall, as distance from the corner. Separation region, reverse flow, and magnification of the turbulent intensity due to the interaction are clearly observed.
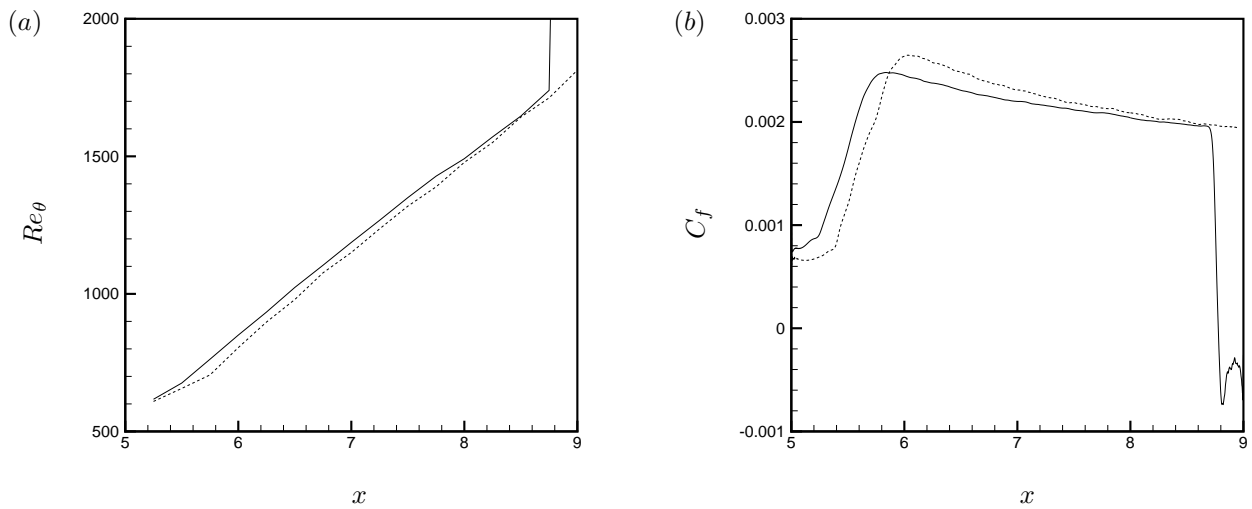
American Institute of Aeronautics and Astronautics

Figure 19. Comparison of mean flow features from simulations with (——) and without (– – – –) the corner. Streamwise variation of (a)Re_θ (based on μ_{wall}) and (b) C_f. In the presence of the corner, transition begins earlier, and the skin friction coefficient is smaller over a part of the domain.
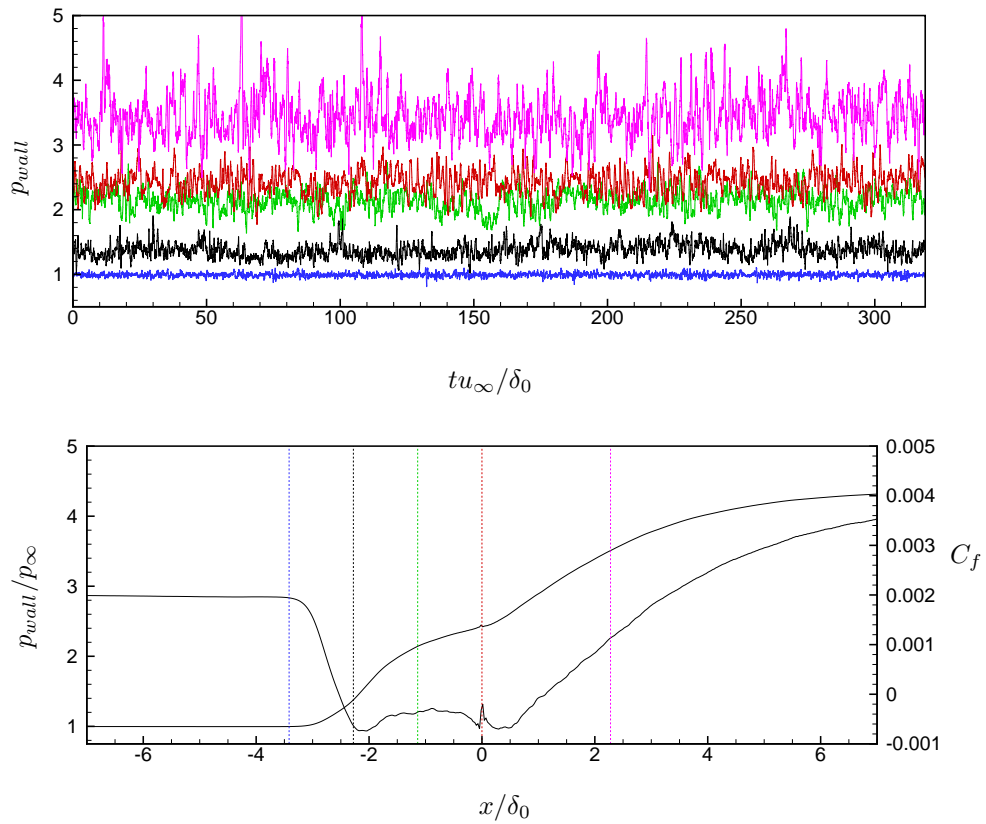

Figure 20. (Top) Time histories of wall pressure at a few locations show the increase in mean pressure as well as lower frequency content through the interaction region. (Bottom) Variation of mean skin friction and wall pressure in the interaction region. Vertical lines indicate the locations corresponding to the time histories in the top figure.

American Institute of Aeronautics and Astronautics

References

[1]Adams, N. A. 2000 Direct simulation of the turbulent boundary layer along a compression ramp at M = 3 and $Re_\theta =$ 1685 *J. Fluid. Mech* **420:**47–83.

[2]Andreopoulos, Y., Agui, J. H. & Briassulis, G. 2000 Shock wave-turbulence interactions *Ann. Rev. Fluid Mech.* **32:**309–345.

[3]Bookey, P. B., Wyckham, C., Smits, A. J. & Martin, M. P. 2005 New Experimental data of STBLI at DNS/LES accessible Reynolds numbers *AIAA Paper* 2005–309.

[4]Degrez, G., Boccadoro, C. H & Wendt, J. F. 1987 The interaction of an oblique shock wave with a laminar boundary layer revisited. An experimental and numerical study *J. Fluid. Mech* **177:** 247–263 .

[5]Delery, J. M & Panaras, A. G. 1996 Shock-Wave/Boundary-Layer Interactions in High-Mach-Number Flows *AGARD AR*–319.

[6]Dolling, D. S. 2001 Fifty Years of Shock-Wave/Boundary-Layer Interaction Research: What Next? *AIAA J.* **39:**1517–1531.

[7]Dolling, D. S. & Murphy, M. T. 1983 Unsteadiness of the separation shock wave structure in a supersonic compressible ramp flowfield *AIAA J.* **21:**1628–1634.

[8]Edwards, J. R. 2008 Numerical simulations of shock/boundary layer interactions using time-dependent modeling techniques: A survey of recent results *Progress in Aerospace Sciences* **44:** 447–465.

[9]Gatski, T. B. & Erlebacher, G. 2002 Numerical simulation of a spatially evolving supersonic turbulent boundary layer *NASA Tech. Memo*–211934.

[10]Guarini, S. E., Moser, R. D., Shariff, K. & Wray, A. 2000 Direct numerical simulation of a supersonic turbulent boundary layer at Mach 2.5 *J. Fluid. Mech.* **414:**1–33.

[11]Knight, D. D. & Degrez, G. 1998 Shock Wave Boundary Layer Interactions in High Mach Number Flows. A Critical Survey of Current Numerical Prediction Capabilities *AGARD AR*–319.

[12]Knight, D. D., Yan, H., Panaras, A.G & Zheltovodov, A. 2003 Advances in CFD prediction of shock wave turbulent boundary layer interactions *Progress in Aerospace Sciences* **39:**121–184.

[13]Kannepalli, C., Arunajatesan. S. & Dash, S. 2002 RANS/LES methodology for supersonic transverse jet interactions with approach flow *AIAA Paper* 2002–1139.

[14]Loginov, M. S., Adams, N. A. & Zheltovodov, A. A. 2006 Large–eddy simulation of shock-wave/turbulent-boundary-layer interaction *J. Fluid. Mech* **565:**135–169.

[15]Morgan, B., Kawai, S. & Lele, S. K. 2010, Large-Eddy simulation of an oblique shock impinging on a turbulent boundary layer *AIAA Paper* 2010–4467.

[16]Park, N. & Mahesh, K. 2007 Numerical and modeling issues in LES of compressible turbulent flows on unstructured grids *AIAA Paper* 2007–722

[17]Priebe, S. & Martin, M. P. 2010 Low–frequency unsteadiness in the DNS of a compression ramp shockwave and turbulent boundary layer interaction *AIAA Paper* 2010–108.

[18]Pirozzoli, S. & Grasso, F. 2006 Direct numerical simulation of impinging shock wave/turbulent boundary layer interaction at M = 2.25 *Phys. Fluids* **18**.

[19]Ringuette, M. J, Bookey, P. B., Wyckham, W. & Smits, A. J. 2009 Experimental study of a Mach 3 compression ramp interaction at $Re_\theta = 2400$ *AIAA J.* **47:**373–385.

[20]Rizzetta, D. & Visbal, M. 2001 Large eddy simulation of supersonic compression ramp flows *AIAA Paper* 2001–2858

[21]Robinet, J. 2007 Bifurcations in shock-wave/laminar-boundary-layer interaction: global instability approach *J. Fluid. Mech.* **579:**85–112.

[22]Schlichting, H.T. 1963 Boundary Layer Theory, McGraw Hill.

[23]Settles, G. S., Fitzpatrick, T. J. & Bogdonoff, S. M. 1979 Detailed Study of Attached and Separated Compression Corner Flowfields in High Reynolds Number Supersonic Flow *AIAA J.* **17:**579-585.

[24]Smits, A. J. & Muck, K. C. 1987 Experimental study of three shock wave/turbulent boundary layer interactions *J. Fluid. Mech* **182:**291–314.

[25]Urbin, G., Knight, D. & Zheltovodov, A. A. 1999 Compressible large eddy simulation using unstructured grid: supersonic turbulent boundary layer and compression corner *AIAA Paper* 1999–0427.

[26]Yee, H. C., Sandham, N. D. & Djomehri, M. J. 1999, Low–dissipative high–order shock–capturing methods using characteristic–based filters *J. Comp. Phys.* **150:** 199–238.

[27]Wu, M & Martin, M. P. 2007 Direct numerical simulation of supersonic turbulent boundary layer over a compression ramp *AIAA J.* **45:**879–889.

[28]Zheltovodov, A. A., Trofimov, V. M., Schulein, E. & Yakovlev, V. N. 1990 An experimental documentation of supersonic turbulent flows in the vicinity of forward- and backward-facing ramps. *Tech. Rep.* 2030. Institute of Theoretical and Applied Mechanics, USSR Academy of Sciences, Novosibirsk.

American Institute of Aeronautics and Astronautics